

# Numerical study on InGaAsN/GaAs multiple-quantum-well laser with GaAsP and GaAsN barriers

Y.-K. Kuo · S.-H. Yen · M.-W. Yao · M.-C. Tsai ·  
M.-L. Chen · B.-T. Liou

Received: 4 March 2008 / Revised version: 7 August 2008 / Published online: 5 September 2008  
© Springer-Verlag 2008

**Abstract** In this work, the multiple-quantum-well InGaAsN laser structures with indirect-GaAsP and direct-GaAsN barriers are investigated by using LASTIP simulation program. We vary the quantum-well number, from 1 to 5, to find appropriate barrier material for InGaAsN laser structures. The simulation results show that InGaAsN laser structure has higher characteristic temperature regardless of what quantum-well number is if the indirect-GaAsP barrier is utilized. Furthermore, for InGaAsN laser structure, the usage of indirect-GaAsP barrier is beneficial for reducing the threshold current when the quantum-well number is from 1 to 2 and the usage of direct-GaAsN barrier is beneficial for reducing the threshold current when the quantum-well number is from 3 to 5.

**PACS** 42.55.Px · 73.40.-c · 78.20.-e · 78.20.Bh

## 1 Introduction

Conventionally, long wavelength InGaAsP laser diode is grown on InP substrate. A highly strained InGaAsN single-

quantum-well (SQW) structure grown on the GaAs substrate was firstly proposed by Kondow et al. in 1995 [1, 2]. The laser diode with GaAs-based InGaAsN material system has higher characteristic temperature than that with conventional InP-based InGaAsP material system. It is because the GaAs-based InGaAsN material system possesses larger conduction band offset. For variant material systems used in optical fiber communication, the corresponding band offset ratio is 79% for InGaAsN/GaAs [3–5], 40% for InGaAsP/InP [6], and 65% for InAsP/InP [6]. As compared with traditional GaAs barrier, the novel GaAsP barrier can reduce carrier leakage due mainly to higher barrier potential and partially compensated tensile strain for InGaAsN quantum well [7–11]. Besides, there are three advantages for using the GaAsN barrier: (i) emitting longer wavelength due to reduced barrier potential; (ii) acting as a source of nitrogen, significantly preventing nitrogen out-diffusion from the well; (iii) achieving a strain-compensated InGaAsN quantum well due to a partially tensile strain in GaAsN barrier [11–13].

It is well-known that the quantum-well number affects the laser performance sufficiently. An appropriate quantum-well number in active region cannot only reduce the thermionic carrier leakage but also improve the uniformity of carrier distribution [14]. Therefore, the barrier potential height and quantum-well number must be optimized to achieve better laser performances.

In this work, the multiple-quantum-well (MQW) InGaAsN laser structures with GaAsP and GaAsN barrier are simulated with LASTIP (LASer Technology Integrated Program) and the quantum-well number is varied from 1 to 5. In addition, the laser performances of the laser structure with different quantum-well numbers are compared and discussed. Previewing the whole manuscript, the relevant numerical parameters and physical models are described

Y.-K. Kuo (✉) · S.-H. Yen · M.-L. Chen  
Department of Physics, National Changhua University  
of Education, Changhua 500, Taiwan  
e-mail: [ykuo@cc.ncue.edu.tw](mailto:ykuo@cc.ncue.edu.tw)  
Fax: +886-4-7211153

M.-W. Yao · M.-C. Tsai  
Institute of Photonics, National Changhua University  
of Education, Changhua 500, Taiwan

B.-T. Liou  
Department of Mechanical Engineering, Hsiuping Institute  
of Technology, Taichung 412, Taiwan

in Sect. 2. In Sect. 3, the comparison between the simulation results and experimental results reported by Liu et al. are presented [15–18]. Furthermore, the threshold currents and corresponding characteristic temperatures of InGaAsN/GaAsP and InGaAsN/GaAsN laser structures are also investigated and compared. In Sect. 4, the appropriate barrier material and quantum-well number for InGaAsN laser diodes are proposed.

## 2 Numerical parameters and physical models

LASTIP [19] is a two-dimensional simulation program that solves Poisson's equation, current continuity equations, photon rate equation, carrier transport equations, and quantum mechanical wave equation. In this study, except the energy bandgap and the effective electron mass, the relevant parameters  $P$  of the  $\text{In}_{1-x}\text{Ga}_x\text{As}_{1-y}\text{N}_y$  material system are linearly interpolated between the parameters of the relevant binary semiconductors. The interpolation formula is written as [20]

$$\begin{aligned} P(\text{In}_{1-x}\text{Ga}_x\text{As}_{1-y}\text{N}_y) \\ = P(\text{Ga}_x\text{In}_{1-x}\text{As}) + P(\text{GaAs}_{1-y}\text{N}_y) - P(\text{GaAs}). \end{aligned} \quad (1)$$

The energy bandgap of  $\text{In}_{1-x}\text{Ga}_x\text{As}_{1-y}\text{N}_y$  material system is expressed by the following equations [21],

$$\begin{aligned} E_g(\text{InGaAsN}) \\ = E_g(\text{term1}) + E_g(\text{term2}) + E_g(\text{bowing}) + E_g(T), \quad (2) \\ E_g(\text{term1}) = x \cdot y \cdot E_g(\text{GaAs}) + x \cdot (1-y) \cdot E_g(\text{GaN}), \quad (3) \\ E_g(\text{term2}) \\ = (1-x) \cdot y \cdot E_g(\text{InAs}) + (1-x) \cdot (1-y) \cdot E_g(\text{InN}), \quad (4) \end{aligned}$$

$$\begin{aligned} E_g(\text{bowing}) \\ = x \cdot y \cdot (1-y) \cdot b(\text{GaAsN}) + y \cdot x \cdot (1-x) \cdot b(\text{InGaAs}), \quad (5) \end{aligned}$$

$$E_g(T) = -5.5 \times 10^{-4} \cdot \left[ \frac{T^2}{T+225} - \frac{300^2}{300+225} \right], \quad (6)$$

where  $T$  is the absolute temperature. The energy bandgaps  $E_g(\text{GaAs})$ ,  $E_g(\text{InAs})$ ,  $E_g(\text{GaN})$ , and  $E_g(\text{InN})$  are 1.424, 0.355, 3.42, and 0.77 eV, respectively. The bowing parameter  $b(\text{GaAsN})$  is  $-18$  eV and  $b(\text{InGaAs})$  is  $-0.6$  eV. In this study, the effective electron mass of InGaAsN is assumed to be  $0.0987m_0$ , where  $m_0$  is the electron mass in free space, which is obtained theoretically with the band-anti-crossing

(BAC) model [22]. Note that the compositions of III and V group atoms in InGaAsN used in the simulation are equal to those used in [22]. Thus, the effective electron mass of InGaAsN obtained in [22] is utilized in this study. Moreover, the  $4 \times 4$  Luttinger–Kohn Hamiltonian including the coupling of the heavy hole and light hole is utilized to evaluate the non-parabolic valence band structures [23]. The strain tensors in the plane of epitaxial growth and its perpendicular direction can be expressed as [21, 24]

$$\varepsilon_{xx} = \varepsilon_{yy} = \frac{a_0 - a}{a}, \quad (7)$$

and

$$\varepsilon_{zz} = -2 \frac{C_{12}}{C_{11}} \varepsilon_{xx}, \quad (8)$$

where  $a_0$  is the lattice constant of substrate,  $a$  is the lattice constant of epitaxial layer,  $C_{11}$  and  $C_{12}$  are the elastic stiffness constants. The strain bulk conduction band is shifted by the energy

$$\delta E_c(x, y) = a_c(\varepsilon_{xx} + \varepsilon_{yy} + \varepsilon_{zz}) = 2a_c \left( 1 - \frac{C_{12}}{C_{11}} \right) \varepsilon, \quad (9)$$

and the strain bulk valence bands are shifted by the energy

$$\delta E_{hh}(x, y) = -P_\varepsilon - Q_\varepsilon, \quad (10)$$

$$\delta E_{lh}(x, y) = -P_\varepsilon + Q_\varepsilon, \quad (11)$$

where

$$P_\varepsilon = -a_v(\varepsilon_{xx} + \varepsilon_{yy} + \varepsilon_{zz}) = -2a_v \left( 1 - \frac{C_{12}}{C_{11}} \right) \varepsilon, \quad (12)$$

$$Q_\varepsilon = -\frac{b}{2}(\varepsilon_{xx} + \varepsilon_{yy} - 2\varepsilon_{zz}) = -b \left( 1 + 2 \frac{C_{12}}{C_{11}} \right) \varepsilon, \quad (13)$$

$a_c$  and  $a_v$  are the conduction-band and valence-band hydrostatic deformation potentials, and  $b$  is the valence-band shear deformation potential. Therefore, the strained bandgaps can be expressed as

$$E_{c-hh}(x, y) = E_g(x, y) + \delta E_c(x, y) - \delta E_{hh}(x, y), \quad (14)$$

and

$$E_{c-lh}(x, y) = E_g(x, y) + \delta E_c(x, y) - \delta E_{lh}(x, y). \quad (15)$$

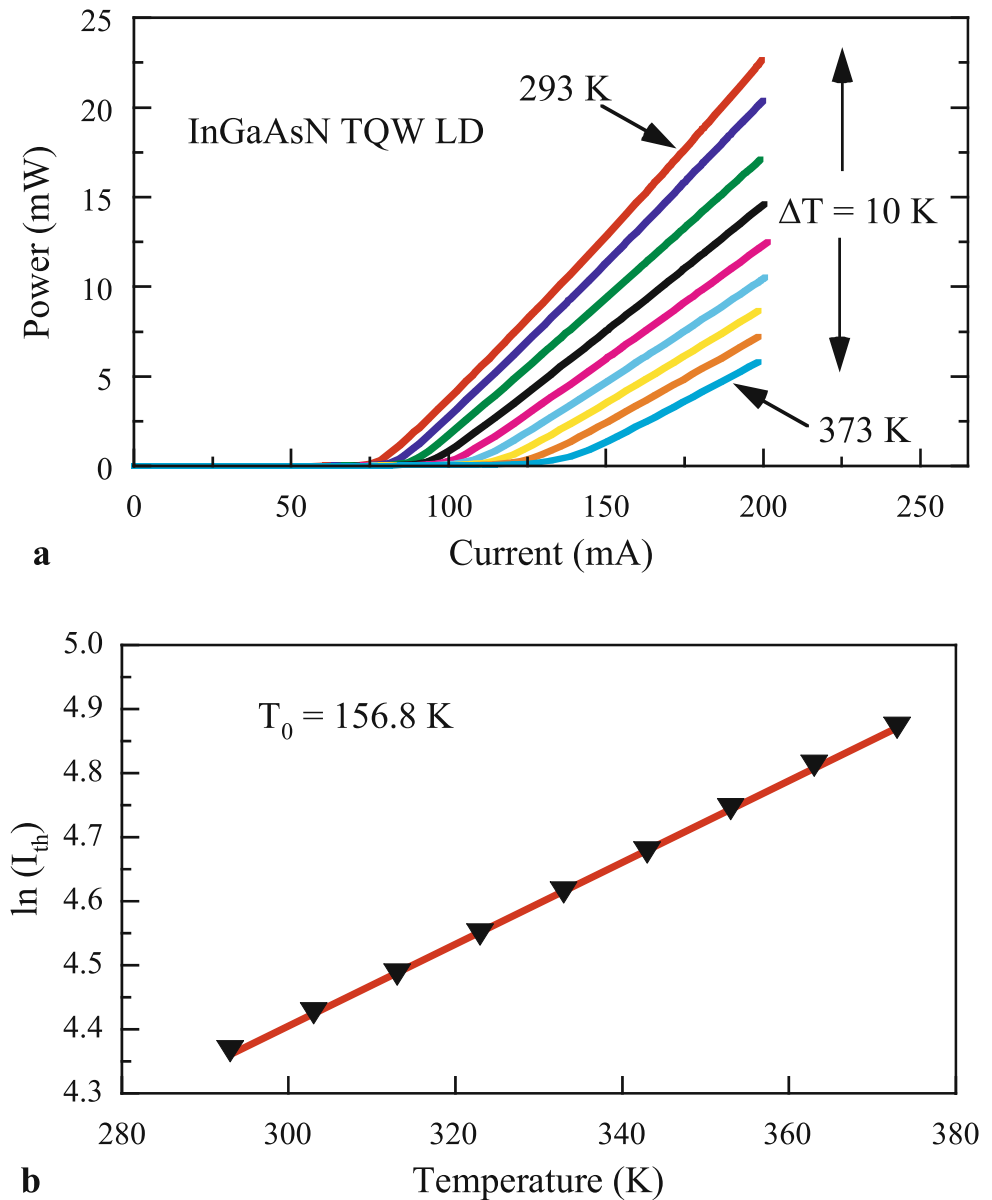
The characteristic temperature of threshold current  $T_0$  can be calculated from [25]

$$I_{\text{th}}(T) = I_0 \exp\left(\frac{T}{T_0}\right), \quad (16)$$

where  $I_0$  is a constant. The Auger recombination rate can be expressed as [26]

$$R_{\text{Auger}} = (C_n n + C_p p) \times (np - n_i^2), \quad (17)$$

**Fig. 1** (a)  $L$ - $I$  performance curves and (b) relationship between  $\ln(I_{th})$  and temperatures obtained from simulation for the InGaAsN laser structure proposed by Liu et al.



where  $C_n$  and  $C_p$  are the Auger coefficients for electrons and holes;  $n$ ,  $p$ , and  $n_i$  are electron density, hole density, and intrinsic carrier density, respectively. The Auger coefficients  $C_n$  and  $C_p$  are assumed to be equal to  $C$  [26]. The temperature dependent Auger coefficient has the form [26, 27]

$$C = C_0 \exp\left(\frac{-E_a}{kT}\right), \quad (18)$$

where  $E_a$  is the activation energy of the Auger process and  $k$  is the Boltzmann constant. The material parameters of the binary semiconductors used in this study, including the Luttinger parameters, elastic stiffness constants, hydrostatic deformation potentials for conduction and valence band, shear deformation potential for valence band, effective masses of

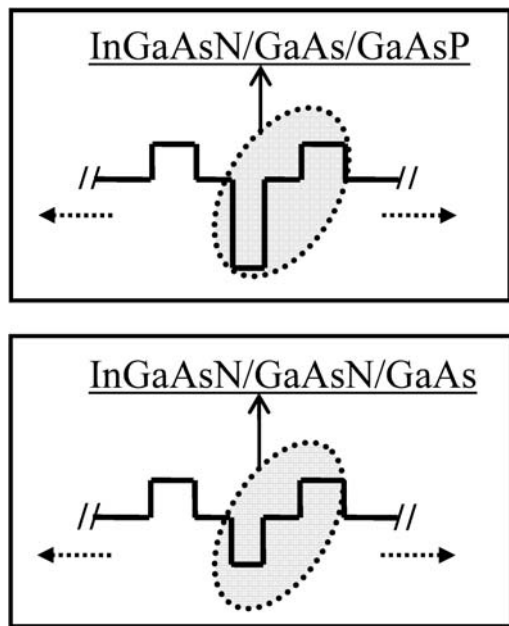
electrons and holes, and lattice constant, are listed in Table 1 [28–33].

### 3 Results and discussion

Referred to the device fabricated by Liu et al. [15–18], the strain-compensated InGaAsN/GaAs/GaAsP triple-quantum-well (TQW) structure is grown on the n-GaAs substrate and has the ridge geometry of  $4 \mu\text{m} \times 1500 \mu\text{m}$ . On the n-GaAs substrate, a  $1.2\text{-}\mu\text{m}$ -thick Si-doped n-type  $\text{Al}_x\text{Ga}_{1-x}\text{As}$  ( $x = 0\text{--}0.5$ ) cladding layer is grown on a  $200\text{-nm}$ -thick n-GaAs buffer layer. Above the n-type cladding layer, the active region is then symmetrically sandwiched between two  $35\text{-nm}$ -thick undoped GaAs waveguide layers. The active region consists of 3 periods  $\text{In}_{0.35}\text{Ga}_{0.65}\text{As}_{0.985}\text{N}_{0.015}$

**Table 1** Material parameters of the binary semiconductors used in this study

Parameter	Symbol (unit)	GaAs	InAs	GaN	InN
Luttinger parameters	$\gamma_1$	6.85	20.4	2.70	3.72
	$\gamma_2$	2.10	8.30	0.76	1.26
	$\gamma_3$	2.90	9.10	1.11	1.63
Elastic stiffness constants	$C_{11}$ ( $10^{11}$ dyn/cm $^2$ )	11.88	8.329	28.2	18.2
	$C_{12}$ ( $10^{11}$ dyn/cm $^2$ )	5.38	4.526	15.9	12.5
Hydrostatic deformation potential for conduction band	$a_c$ (eV)	-9.70	-6.08	-6.71	-2.65
Hydrostatic deformation potential for valence band	$a_v$ (eV)	-1.16	-1.00	-0.69	-0.7
Shear deformation potential for valence band	$b$ (eV)	-1.70	-1.80	-1.7	-1.20
Electron effective mass	$m_e/m_0$	0.067	0.023	0.15	0.07
Heavy-hole effective mass	$m_{hh}/m_0$	0.50	0.40	0.80	0.80
Lattice constant	$a$ (Å)	5.653	6.0584	4.52	4.98

**Fig. 2** Schematic conduction band diagram of InGaAsN/GaAs/GaAsP and InGaAsN/GaAsN/GaAs structures

(6.4 nm)/GaAs(7 nm)/GaAs<sub>0.82</sub>P<sub>0.18</sub>(8 nm) quantum well region, which are sandwiched between two 12-nm-thick GaAs<sub>0.82</sub>P<sub>0.18</sub> tensile-strained barrier layers. A 1.2-μm-thick C-doped p-type Al<sub>x</sub>Ga<sub>1-x</sub>As ( $x = 0.5\text{--}0$ ) upper cladding layer is grown above the active region, and followed by a 200-nm-thick p<sup>+</sup>-GaAs cap layer.

Figure 1(a) shows the  $L$ - $I$  curves obtained from simulation, which are close to the experimental results proposed by Liu et al. [15]. According to Fig. 1(a), the plot of  $\ln(I_{th})$  versus temperature is plotted in Fig. 1(b). The characteristic temperature curve-fitted by using (16) is 156.8 K in the op-

erating temperature range of 293 to 353 K. This is close to the experimental value 157.2 K [15].

An idea of designing InGaAsN/(In)GaAsN/GaAs MQW structure was proposed by Jouhti et al. [34]. Based on the concept proposed by them, a new structure with 3 periods In<sub>0.35</sub>Ga<sub>0.65</sub>As<sub>0.985</sub>N<sub>0.015</sub>(6.4 nm)/GaAs<sub>0.99</sub>N<sub>0.01</sub>(7 nm)/GaAs(8 nm) quantum well region is compared with the original structure proposed by Liu et al. The schematic conduction band diagrams of these two structures are shown in Fig. 2. Here, the GaAs/GaAs<sub>0.82</sub>P<sub>0.18</sub> barrier is denoted as indirect-GaAsP barrier because the GaAsP is not aligned with InGaAsN quantum well directly. On the other hand, the GaAs<sub>0.99</sub>N<sub>0.01</sub>/GaAs barrier is denoted as direct-GaAsN barrier because the GaAsN is directly aligned with InGaAsN quantum well. Note that, besides the active region, other layers in these two structures are the same.

The gain spectra are shown in Fig. 3. The peaks of wavelengths for the InGaAsN quantum well with indirect-GaAsP barriers are 1.2875 μm at 293 K and 1.3395 μm at 373 K. Meanwhile, the peaks of wavelengths for the InGaAsN quantum well with direct-GaAsN barriers are 1.3079 μm at 293 K and 1.3649 μm at 373 K. Specifically, the temperature dependent wavelength,  $d\lambda/dT$ , for the InGaAsN quantum well with indirect-GaAsP and direct-GaAsN barriers are 0.65 nm/K and 0.71 nm/K, respectively. In addition, the conduction band offsets for the InGaAsN quantum well with indirect-GaAsP and direct-GaAsN barriers are 403 and 135 meV; the valence band offsets for the InGaAsN quantum well with indirect-GaAsP and direct-GaAsN barriers are 173 and 120 meV. The valence subbands for the InGaAsN quantum well with indirect-GaAsP and direct-GaAsN barriers are shown in Fig. 4, where the abscissa  $k_t$  is the in-plane wave vector perpendicular to the crystal growth

**Fig. 3** Gain spectra for the InGaAsN quantum well with indirect-GaAsP and direct-GaAsN barriers

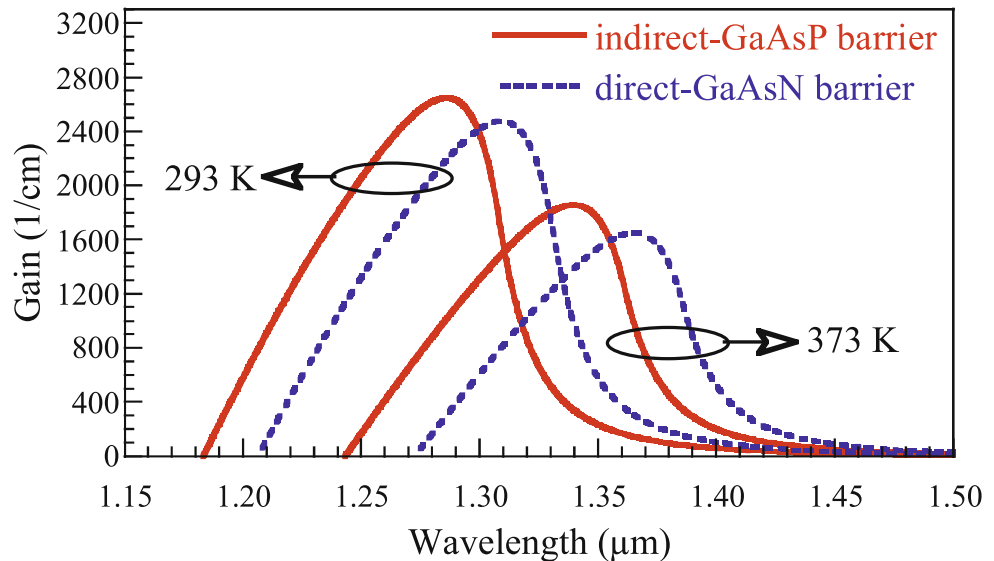
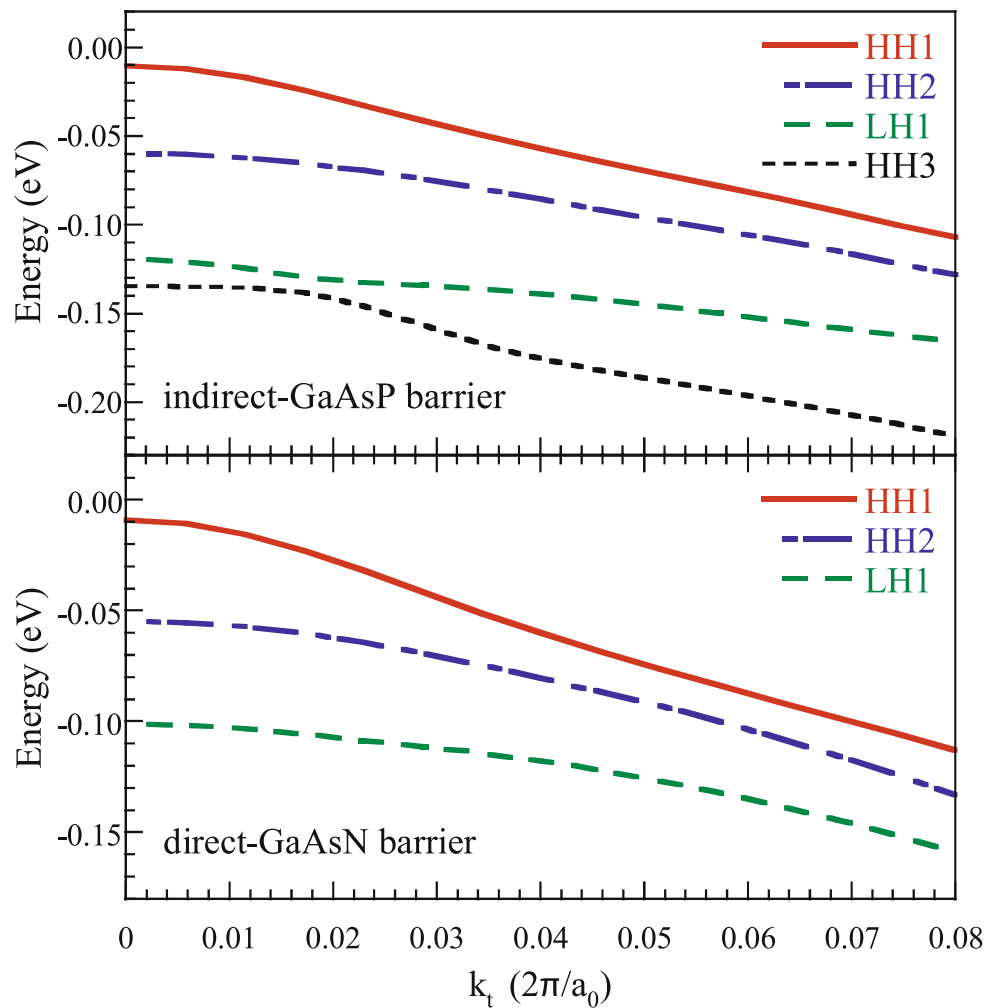


**Fig. 4** Valence subbands for the InGaAsN quantum well with indirect-GaAsP and direct-GaAsN barriers



direction and the 0 eV point in the valence band structure is related to the highest point of valence band at strain-free condition. More valence subbands in the quantum well are

predicted to have stronger hole confinement. However, the larger threshold current caused by more valence subbands is also obtained [35]. As shown in Fig. 4, the structure with

**Fig. 5**  $L-I$  performance curves of SQW structures with indirect-GaAsP and direct-GaAsN barriers

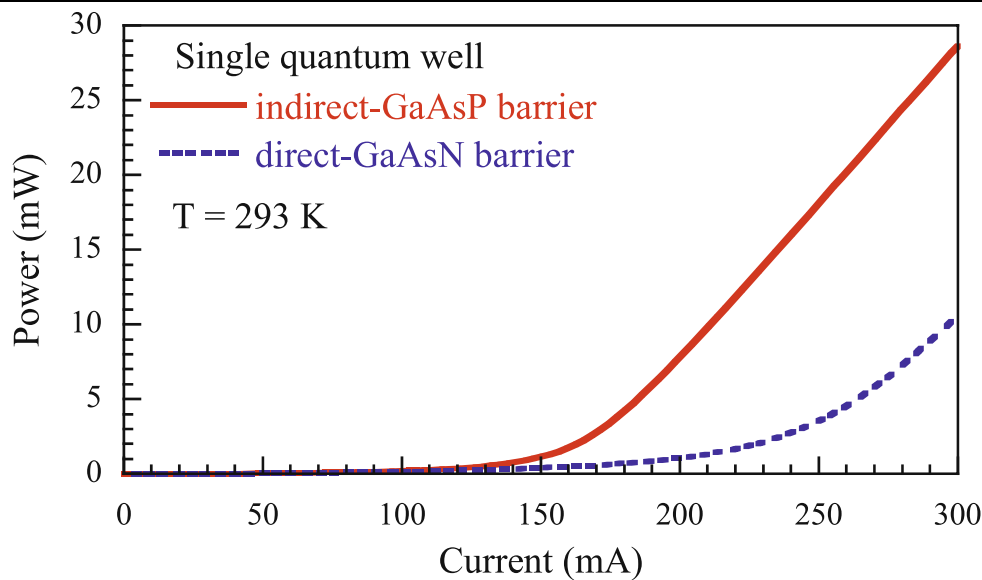
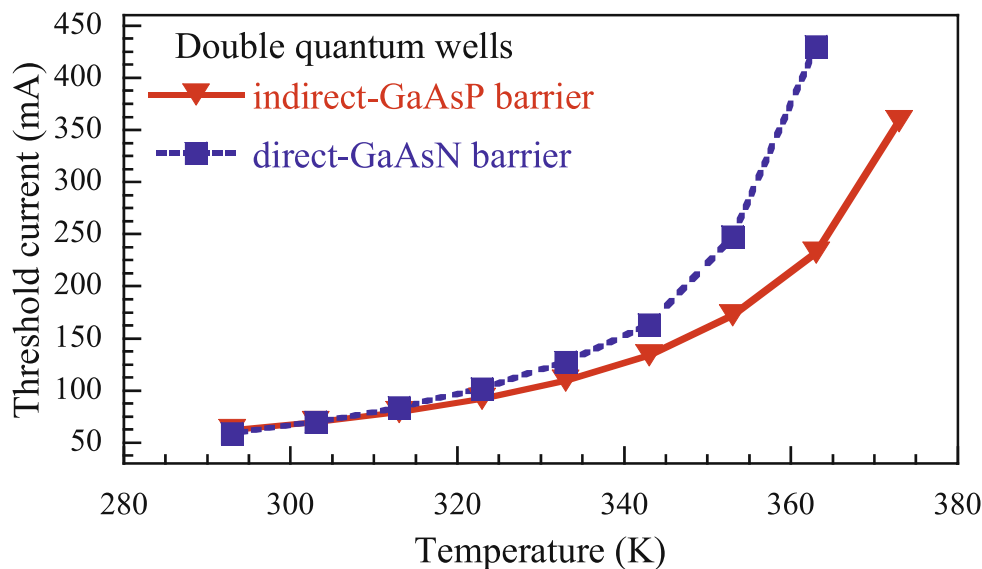


**Fig. 6** Threshold current versus operating temperature for DQW structures with indirect-GaAsP and direct-GaAsN barriers



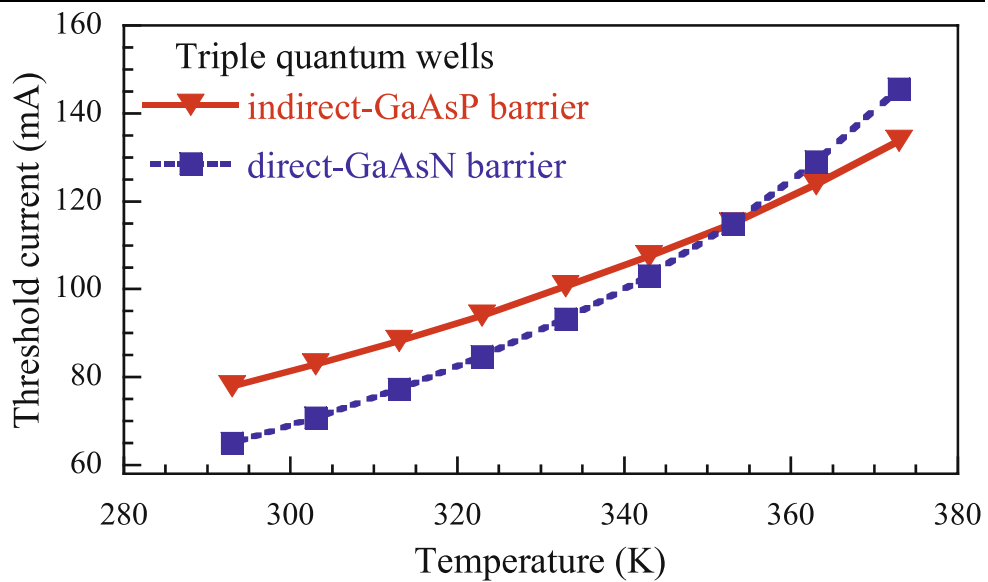
indirect-GaAsP barrier has more valence subbands in the quantum well than that with direct-GaAsN barriers due to its higher barrier potential. Comparison of the structures with indirect-GaAsP and direct-GaAsN barriers, the former may have larger threshold current and better hole confinement.

Our subsequent investigation is to compare which barrier, indirect-GaAsP or direct-GaAsN, is better for the InGaAsN laser structure when the quantum-well number is varied from 1 to 5. At first, as shown in Fig. 5, the  $L-I$  curves of SQW structures with indirect-GaAsP and direct-GaAsN barriers are plotted. It indicates that the structure with indirect-GaAsP barrier has lower threshold current than that with direct-GaAsN barrier at operating temperatures is 293 K. Presumably, this is because the structure with indirect-GaAsP barrier has larger barrier potential to suppress the carrier leakage. Therefore, the indirect-GaAsP bar-

rier is suggested to be utilized for the SQW InGaAsN laser structure.

The threshold current versus operating temperature for double-quantum-well (DQW) structures with indirect-GaAsP and direct-GaAsN barriers is plotted in Fig. 6. It is shown that the threshold current of structure with direct-GaAsN barrier is a little smaller than that with indirect-GaAsP barrier as the operating temperature is below 303 K. Specifically, as operating temperature is higher than 303 K, the threshold current of structure with direct-GaAsN barrier increases rapidly; in the mean time, it is much more sensitive to temperature. It is presumably the thermionic carrier leakage of the structure with direct-GaAsN barrier is serious due to its smaller barrier potential. On the contrary, the thermionic carrier leakage could be suppressed successfully for the structure with indirect-GaAsP barriers. Therefore,

**Fig. 7** Threshold current versus operating temperature for TQW structures with indirect-GaAsP and direct-GaAsN barriers



for DQW InGaAsN laser structures, the indirect-GaAsP barriers are also suggested to be utilized. However, for the double-quantum-well laser structures with indirect-GaAsP and direct-GaAsN barriers, due to large electron leakage current and poor carrier confinement in the conduction band, the threshold current increases rapidly as the temperature is higher than 353 K.

Figure 7 shows the threshold current versus operating temperature for triple-quantum-well structures with indirect-GaAsP and direct-GaAsN barriers. It is found that the structure with indirect-GaAsP barrier has larger threshold current when the operating temperature is ranging from 293 to 353 K, while the structure with direct-GaAsN barrier has larger threshold current when the operating temperature is higher than 353 K. The larger threshold current of structure with indirect-GaAsP barrier may be resulted from more valance subbands in quantum wells as shown in Fig. 4. Compared with the DQW structure with direct-GaAsN barrier, the threshold current of the TQW structure with direct-GaAsN barrier does not increase rapidly as the DQW structure does. However, as shown in Fig. 7, the increasing of threshold current for the structure with direct-GaAsN barrier is rapider than that with indirect-GaAsP barrier. Presumably, this is because of the increasing of Auger recombination rate as shown in Figs. 8(a) and 8(b). As the operating temperature increases from 293 to 353 K, the Auger recombination rate increases 2.18 times for the structure with indirect-GaAsP barrier and 2.85 times for that with direct-GaAsN barrier. Therefore, for the TQW InGaAsN laser structure, the design of direct-GaAsN barrier is more appropriate due to much lower threshold current.

The threshold current versus operating temperature for the structure with 4 quantum wells is plotted in Fig. 9. As the operating temperature is ranging from 293 to 373 K,

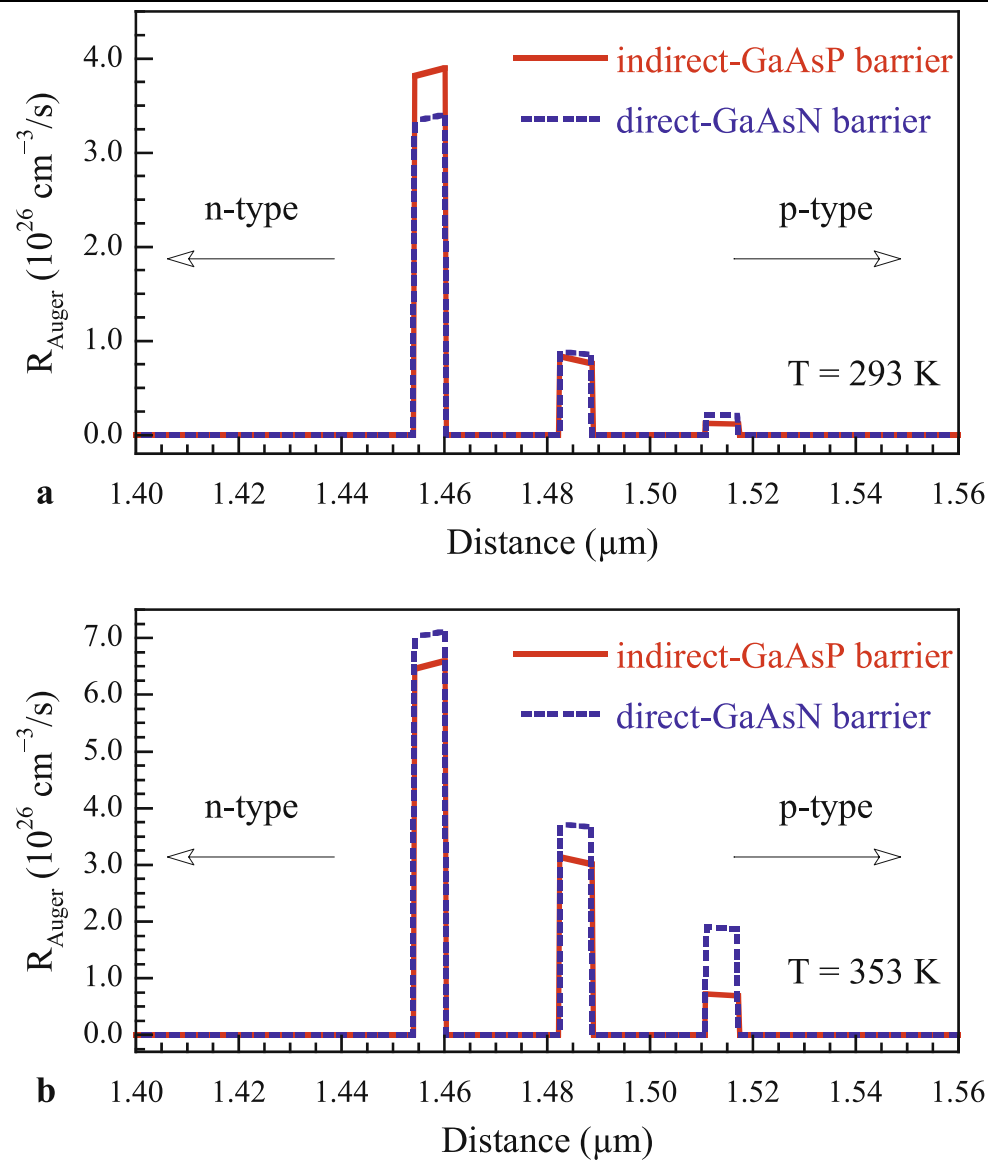
the structure with indirect-GaAsP barrier possesses larger threshold current due to more valance subbands in quantum wells. The Auger recombination rates at 293 and 353 K are shown in Figs. 10(a) and 10(b), respectively. As the operating temperature increases from 293 to 353 K, the Auger recombination rate increases 1.50 times for structure with indirect-GaAsP barriers and 2.37 times for that with direct-GaAsN barriers. Furthermore, the threshold current of five-quantum-well structure versus operating temperature is shown in Fig. 11. According to the simulation results, for both four-quantum-well and five-quantum-well InGaAsN laser structures, the utilization of direct-GaAsN barrier is beneficial for reducing the threshold current. It is evident that when the number of quantum wells is larger than 2, the threshold current does not increase rapidly when the temperature increases due to effectively improved carrier confinement in the conduction band.

Table 2 lists the characteristic temperatures of different quantum-well-number structures with indirect-GaAsP and direct-GaAsN barriers as the operating temperature is ranging from 293 to 353 K. In the table, the characteristic temperature of SQW structure is omitted due to poor laser performance as the operating temperature is above 293 K. The characteristic temperature of the structure with indirect-GaAsP barrier is larger than that with direct-GaAsN barrier no matter what quantum-well number is. This is due mainly to the higher barrier potential of indirect-GaAsP and the reduced thermionic carrier leakage.

#### 4 Conclusion

In this work, referred to a real device, the MQW InGaAsN laser structures with indirect-GaAsP and direct-GaAsN bar-

**Fig. 8** Auger recombination rates of TQW in the epitaxial growth direction as operating temperature is (a) 293 K and (b) 353 K. The abscissa is the distance along growth direction and the origin is located at the bottom of the substrate



**Fig. 9** Threshold current versus operating temperature for the structure with 4 quantum wells

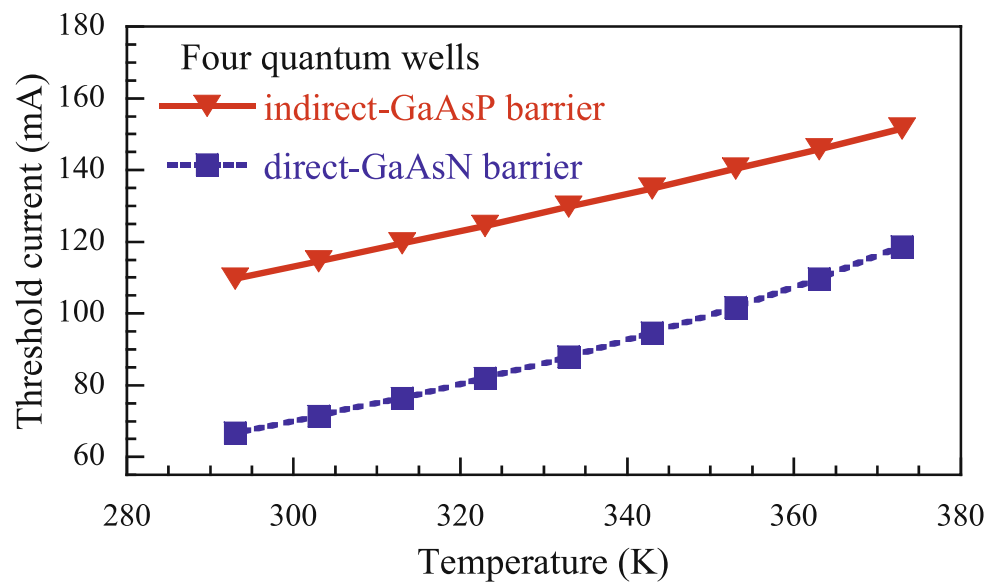


**Fig. 10** Auger recombination rates of four-quantum-well structures in the epitaxial growth direction as operating temperature is (a) 293 K and (b) 353 K. The abscissa is the distance along growth direction and the origin is located at the bottom of the substrate

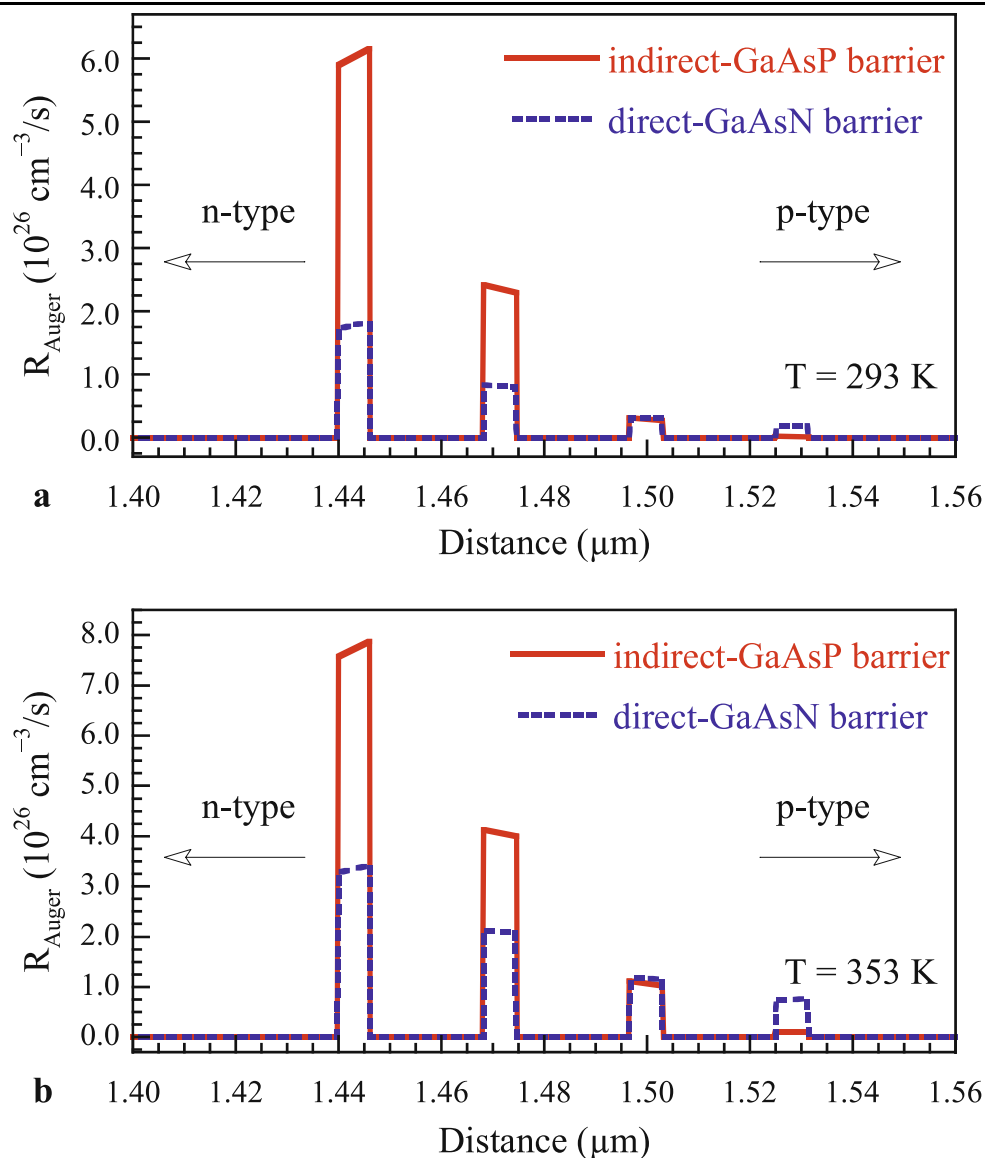


**Fig. 11** Threshold current versus operating temperature for the structure with 5 quantum wells

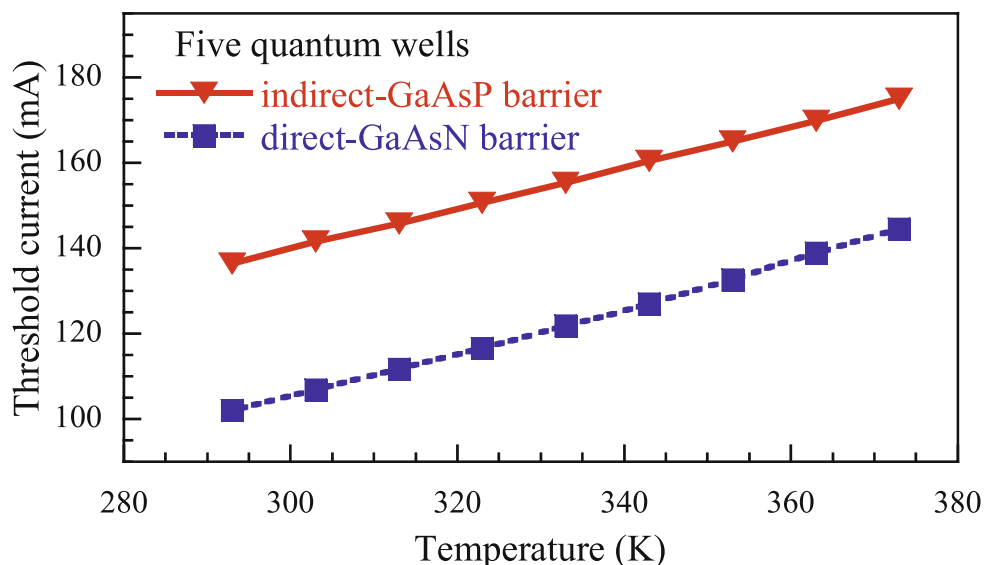


**Table 2** Characteristic temperatures of different quantum-well-number structures with indirect-GaAsP and direct-GaAsN barriers

Barrier	Characteristic temperature (K)				
	SQW	DQWs	TQWs	Four QWs	Five QWs
Indirect-GaAsP	—	47.8	149.0	249.1	323.2
Direct-GaAsN	—	37.4	99.8	139.1	230.3

riers are studied and compared with LASTIP simulation program. Meanwhile, the quantum-well number is varied from 1 to 5. The simulation results indicate that the InGaAsN laser structure with indirect-GaAsP barrier possesses higher characteristic temperature than that with direct-GaAsN barrier. If the number of quantum wells for the InGaAsN laser structures with indirect-GaAsP and direct-GaAsN barriers is 1 or 2, due to large electron leakage current, the threshold current increases rapidly as the temperature increases. If the number of quantum wells is larger than 2, the threshold current does not increase markedly as the temperature increases due to effective carrier confinement in the conduction band. Furthermore, for InGaAsN laser structure, the usage of indirect-GaAsP barrier is beneficial for reducing the threshold current when the quantum-well number is from 1 to 2 while the usage of direct-GaAsN barrier is beneficial for reducing the threshold current when the quantum-well number is from 3 to 5.

**Acknowledgements** This work is supported by the National Science Council of Taiwan under grant NSC 96-2112-M-018-007-MY3.

## References

- M. Kondow, K. Uomi, A. Niwa, T. Kitatani, S. Watahiki, Y. Yazawa, Jpn. J. Appl. Phys. **35**, 1273 (1996)
- M. Kondow, T. Kitatani, S. Nakatsuka, M.C. Larson, K. Nakahara, Y. Yazawa, M. Okai, K. Uomi, IEEE J. Select. Top. Quantum Electron. **3**, 719 (1997)
- M. Hetterich, M.D. Dawson, A.Yu. Egorov, D. Bernklau, H. Riechert, Appl. Phys. Lett. **76**, 1030 (2000)
- G. Dumitras, H. Riecher, J. Appl. Phys. **94**, 3955 (2003)
- J.C.L. Yong, J.M. Rorison, M. Othman, H.D. Dawson, K.A. Williams, IEE Proc. Optoelectron. **150**, 80 (2003)
- Y.G. Zhang, J.X. Chen, Y.Q. Chen, M. Qi, A.Z. Li, K. Fröjd, B. Stoltz, J. Cryst. Growth **227**, 329 (2001)
- H.Q. Hou, K.D. Choquette, K.M. Geib, B.E. Hammons, IEEE Photonics Technol. Lett. **9**, 1057 (1997)
- M. Hetterich, M.D. Dawson, A.Yu. Egorov, D. Bernklau, H. Riechert, S.W. Bland, J.I. Davies, M.D. Geen, in *Proc. 12th Annual Meeting IEEE Lasers and Electro-Optics Society (LEOS)*, San Francisco, California, vol. 1, p. 368 (1999)
- W. Li, J. Turpeinen, P. Melanen, P. Savolainen, P. Uusimaa, M. Pessa, Appl. Phys. Lett. **78**, 91 (2001)
- N. Tansu, J.Y. Yeh, L.J. Mawst, J. Phys.: Condens. Matter **16**, S3277 (2004)
- Y. Qu, C.Y. Liu, S. Yuan, Appl. Phys. Lett. **85**, 5149 (2004)
- W. Li, T. Jouhti, C.S. Peng, J. Konttinen, P. Laukkanen, E.M. Pavelescu, M. Dumitrescu, M. Pessa, Appl. Phys. Lett. **79**, 3386 (2001)
- N. Tansu, J.Y. Yeh, L.J. Mawst, Appl. Phys. Lett. **83**, 2512 (2003)
- M.N. Akram, O. Kjebon, S. Marcinkevičius, R. Schatz, J. Berggren, F. Olsson, S. Lourdudoss, IEEE J. Quantum Electron. **42**, 713 (2006)
- C.Y. Liu, S.F. Yoon, W.J. Fan, A. Uddin, S. Yuan, IEEE Photonics Technol. Lett. **18**, 791 (2006)
- C.Y. Liu, Y. Qu, S. Yuan, S.F. Yoon, Appl. Phys. Lett. **85**, 4594 (2004)
- Y. Qu, C.Y. Liu, S.G. Ma, S. Yuan, B. Bo, G. Liu, H. Jiang, IEEE Photonics Technol. Lett. **16**, 2406 (2004)
- C.Y. Liu, S.F. Yoon, S.Z. Wang, W.J. Fan, Y. Qu, S. Yuan, IEEE Photonics Technol. Lett. **16**, 2409 (2004)
- LASTIP by Crosslight Software, Inc. Burnaby, Canada (2005) <http://www.crosslight.com>
- G. Lin, C.P. Lee, Opt. Quantum Electron. **34**, 1191 (2002)
- Y.A. Chang, H.C. Kuo, Y.H. Chang, S.C. Wang, Opt. Commun. **241**, 195 (2004)
- S.T. Ng, W.J. Fan, S.F. Yoon, S.Z. Wang, Y. Qu, C.Y. Liu, S.G. Ma, S. Yuan, J. Appl. Phys. **96**, 4663 (2004)
- C.Y.P. Chao, S.L. Chuang, Phys. Rev. B **46**, 4110 (1992)
- J. Minch, S.H. Park, T. Keating, S.L. Chuang, IEEE J. Quantum Electron. **35**, 771 (1999)
- S.R. Selmic, T.M. Chou, J. Sih, J.B. Kirk, A. Mantie, J.K. Butler, D. Bour, G.A. Evans, IEEE J. Select. Top. Quantum Electron. **7**, 340 (2001)
- J. Piprek, J.K. White, A.J. SpringThorpe, IEEE J. Quantum Electron. **38**, 1253 (2002)
- T.J. Houle, J.C.L. Yong, C.M. Marinelli, S. Yu, J.M. Rorison, I.H. White, J.K. White, A.J. SpringThorpe, B. Garrett, IEEE J. Quantum Electron. **41**, 132 (2005)
- S.A. Choulis, T.J.C. Hosea, S. Tomić, M. Kamal-Saadi, A.R. Adams, E.P. O'Reilly, B.A. Weinstein, P.J. Klar, Phys. Rev. B **66**, 165321 (2002)
- I. Vurgaftman, J.R. Meyer, J. Appl. Phys. **94**, 3675 (2003)
- I. Vurgaftman, J.R. Meyer, L.R. Ram-Mohan, J. Appl. Phys. **89**, 5815 (2001)
- G. Leibiger, V. Gottschalch, M. Schubert, J. Appl. Phys. **90**, 5951 (2001)
- A.T. Meney, E.P. O'Reilly, A.R. Adams, Semicond. Sci. Technol. **11**, 897 (1996)
- M.C.Y. Chan, C. Surya, P.K.A. Wai, J. Appl. Phys. **90**, 197 (2001)
- T. Jouhti, C.S. Peng, E.M. Pavelescu, J. Konttinen, L.A. Gomes, O.G. Okhotnikov, M. Pessa, IEEE J. Select. Top. Quantum Electron. **8**, 787 (2002)
- J.C.L. Yong, J.M. Rorison, I.H. White, IEEE J. Quantum Electron. **38**, 1553 (2002)